Tropical Cyclones in Global Storm-Resolving Models

Falko Judt

National Center for Atmospheric Research, Boulder, Colorado, USA

and

Daniel Klocke[8], Rosimar Rios-Berrios[1], Benoit Vanniere[13], Florian Ziemen[3]

and

Ludovic Auger[2], Joachim Biercamp[3], Christopher Bretherton[4], Xi Chen[5], Peter Düben[6], Cathy Hohenegger[10], Marat Khairoutdinov[7], Chihiro Kodama[9], Luis Kornblueh[10], Shian-Jiann Lin[5], Masuo Nakano[9], Philipp Neumann[14], William Putman[11], Niklas Röber[3], Malcom Roberts[15], Masaki Satoh[12], Ryosuke Shibuya[12], Bjorn Stevens[10] , Pier Luigi Vidale[13], Nils Wedi[6], Linjiong Zhou[5],

[1]National Center for Atmospheric Research, P.O. Box 3000, Boulder, CO 80307, USA

[2]CNRM Meteo-France, 42 av. G. Coriolis, 31057 Toulouse, France

[3]German Climate Computing Center, DKRZ, Bundesstraße 45a, 20146, Hamburg, Germany

[4]Department of Atmospheric Sciences, University of Washington, Box 351640, Seattle, WA, 98195, USA

[5]Geophysical Fluid Dynamics Laboratory, Princeton University, Forrestal Campus/U.S. Route 1, P.O. Box 308, Princeton, NJ, 08542, USA

[6]ECMWF, Shinfield Road, Reading, RG2 9AX, UK

[7]School of Marine and Atmospheric Sciences, Stony Brook University, Stony Brook, NY, 11794, USA

[8]Hans-Ertel-Zentrum für Wetterforschung, Deutscher Wetterdienst, Frankfurter Straße 135, 63067 Offenbach, Germany

[9]Japan Agency for Marine-Earth Science and Technology, 3173-15, Showa-machi, Kanazawa-ku, Yokohama, Kanagawa, 236-0001, Japan

[10]Max Planck Institute for Meteorology, Bundesstraße 53, 20146 Hamburg, Germany

[11] *NASA Global Modeling and Assimilation Office, Goddard Space Flight Center, Greenbelt, Maryland, USA*
[12] *Atmosphere and Ocean Research Institute, The University of Tokyo, 5-1-5 Kashiwanoha, Kashiwa, Chiba, 277-8564, Japan*
[13] *National Centre for Atmospheric Science, University of Reading, Reading, UK*
[14] *Helmut-Schmidt-Universität, Fakultät für Maschinenbau, High Performance Computing, Holstenhofweg 85, 22043 Hamburg, Germany*
[15] *UK Met Office, Fitzroy Rd, Exeter EX1 3PB, United Kingdom*

June 23, 2020

Corresponding author: Falko Judt, National Center for Atmospheric Research, P.O. Box 3000, Boulder, CO 80307, USA.
E-mail: fjudt@ucar.edu

Abstract

Recent progress in computing and model development has initiated the era of global storm-resolving modeling and with it the potential to transform weather and climate prediction. Within the general theme of vetting this new class of models, the present study evaluates nine global-storm resolving models in their ability to simulate tropical cyclones. Results show that, broadly speaking, the models produce realistic tropical cyclones and remove longstanding issues known from global models such as the deficiency to accurately simulate TC intensity. However, TCs are strongly affected by model formulation, and all models suffer from unique biases regarding the number of cyclones, intensity, size, and structure. Some models simulated TCs better than others, but no single model was superior in every way. The overall results indicate that global storm-resolving models are able to open a new chapter in tropical cyclone prediction, but they need to be improved to unleash their full potential.

Keywords tropical cyclone; typhoon; hurricane; global cloud-resolving model; tropical meteorology; numerical modeling; model verification; predictability

1. Introduction

Tropical cyclones (TCs) are among the most destructive natural hazards, and predicting TCs is an important task of weather and climate models. Moreover, TCs are optimal testbeds for assessing the quality of numerical models, because their unique dynamics reveal deficiencies in the model formulation through artifacts such as unrealistic structure. The overall purpose of the present study is to evaluate a new class of atmosphere models—global storm-resolving models (Satoh et al. 2019)—in their ability to simulate TCs. Specifically, we report on TC-related achievements, deficiencies, and biases in nine global storm-resolving models, and we hope that our findings will pave the way for improving the next generation of weather and climate models.

Global models have been a vital instrument in TC prediction although they have not been able to accurately predict TC intensity. A decade ago, Hamill et al. (2011) reported that global weather models, which at that time had mesh spacings between 50–150 km, were plagued by wind speed biases of down to -30 m s^{-1}. Even though some progress has been made, the most recent model with mesh spacings of 10–25 km still fail to capture the high winds of TCs (e.g., Magnusson et al. 2019; Hodges and Klingaman 2019; Roberts et al. 2020). One of the main reasons for this shortcoming is insufficient horizontal resolution (Davis 2018). In fact, years of research with regional models have documented that storm-resolving resolution, here defined as <5 km, is necessary to accurately simulate the inner-core structure of TCs (e.g., Chen et al. 2007; Gentry and Lackmann 2010), which in turn is necessary to predict TC intensity (e.g., Davis et al. 2008; Gopalakrishnan et al. 2012; Fox and Judt 2018).

The preceding arguments suggest that global storm-resolving models are ideal tools for TC prediction, because they combine the advantages of current-generation global and regional models, that is, they offer global coverage *and* storm-resolving horizontal resolution. Indeed, there has been some qualitative evidence that global storm-resolving models capture the inner-core structure of TCs quite realistically (e.g., Fudeyasu et al. 2008; Zhou et al. 2019). Other studies have demonstrated that models with 7–10 km mesh spacings reduce some of the biases found in coarser-resolution models (Manganello et al. 2012; Nakano et al. 2017). However, the immense computational resources needed to run global models with mesh spacings of $\leq$5 km have so far precluded a detailed, TC-focused evaluation of those models. The present study attempts to fill this gap by evaluating the models that participated in the DYAMOND initiative (Stevens et al. 2019), and it expands on the brief overview of TCs already presented in Stevens et al. (2019).

Given computational limitations and the general purpose of DYAMOND, each participating model provided only one 40-day simulation. This means that it was not possible to evaluate the models as usually done in the weather prediction community, i.e., by computing errors of metrics such as maximum wind speed from a large number of short-range forecasts (e.g., DeMaria et al. 2014; Nakano et al. 2017). It was also not possible to evaluate long-term TC climatologies as in climate studies (e.g., Camargo et al. 2005; Bengtsson et al. 2007; Manganello et al. 2012; Roberts et al. 2020). Instead, we focused on answering the following questions:

- What are the biases in TC number, tracks, intensity, and size over those 40 days?
- Do the models produce TCs with a realistic structure?
- Do the models have similar biases, or does each model have its own?

The validity of the study rests on three important assumptions, namely (i) the 40-day period of DYAMOND is sufficient to draw general conclusions about the TC characteristics in each model, (ii) objects identified as TCs by the tracking software (see section 2) would also be identified as TCs by human forecasters (and vice versa), and (iii) the observations used to evaluate the models are sufficiently accurate.

We are confident that (i) holds true because the discrepancies between the models were substantial and almost certainly caused by different model formulations. Furthermore, even though 40 days is relatively short, we have global statistics, and the sampling is not as sparse as one might intuit. It is more difficult to judge the validity of (ii) and (iii), but given the amount of past studies that relied on those assumptions, we assumed they would hold for this work, too.

Lastly, we emphasize that high horizontal resolution is necessary but not sufficient for accurately simulating TC structure and intensity. Advances in ocean coupling and model physics are critical as well (e.g., Lee and Chen 2014; Mogensen et al. 2017; Magnusson et al. 2019). One area that seems to be particularly important is the parameterization of the boundary layer (Kanada et al. 2012; Kepert 2012; Zhang et al. 2015) and the surface layer, especially the drag (Zeng et al. 2010; Green and Zhang 2013; Magnusson et al. 2019).

The remainder of the paper is structured as follows: in section 2, we present the data and methods. Section 3 contains the results, organized into subsections on (i) TC number and tracks, (ii) intensity, (iii) size, (iv) structure, and (v) the sensitivity of TCs on resolution and parameterized convection. The findings are discussed in section 4 and the paper ends with a summary and conclusions in section 5.

2. Data and Methods

This study leverages the vast data repository of DYAMOND, which contains the output from the following nine global models: ARPEGE, FV3, GEOS, ICON, IFS[1], MPAS, NICAM, SAM, and UM. For details about the DYAMOND experiment and the participating models see Stevens et al. (2019) and references therein. The models were run on meshes with maximum spacings between 2.5 km (ARPEGE, ICON) and 7.8 km (UM). All models except GEOS were initialized with the 00 UTC 1 August 2016 analysis from the *European Centre for Medium-Range Weather Forecasts (ECMWF)* and integrated for 40 days (1 August–10 September 2016). The sea surface temperature and sea ice fields were prescribed using 7-day running mean analyses from *ECMWF*.

To identify TCs in the model output, we employed the *GFDL vortex tracker* (Marchok 2002; Biswas et al. 2018). This software searches for TCs based on spatial minima and maxima in the following fields: (i) relative vorticity at 10 m, (ii) sea-level pressure, (iii) wind speed at 10 m, 850

[1] The IFS model considered here is an experimental version of the operational IFS model with 4-km mesh spacing and explicitly simulated deep convection

hPa, and 700 hPa, and (iv) layer-mean temperature between 300-500 hPa (Marchok 2002). The tracker produces *track files* with 6-hourly *records* that contain TC location (latitude/longitude), maximum 10-m wind speed (v_{max}), minimum sea-level pressure (p_{min}), and wind radii r_{17}, r_{25}, and r_{32}, i.e., the maximum radial extent of 17 m s^{-1}, 25 m s^{-1}, and 32 m s^{-1} winds in each compass quadrant (northeast, southeast, southwest, and northwest).

To evaluate the models, we used best track data from the International Best Track Archive for Climate Stewardship [IBTrACS version 4; Knapp et al. (2010, 2018)]. Specifically, we used the data from the WMO agency responsible for a given storm, and we accounted for wind speed reporting differences by converting all v_{max} values to 1-min sustained winds following Harper et al. (2008). Note that the IBTrACS data does not contain direct observations or objective analyses, but subjective analyses from human forecasters based on available but limited observations. For simplicity, we will nevertheless refer to the IBTrACS data as "observations".

For a number of reasons, the workflow was not trivial. For example, some groups provided the output on their native model mesh, which rendered the data unreadable for the tracker. Furthermore, the high-resolution output caused the tracker to falsely identify hundreds of convective objects as TCs. To overcome those issues, we carried out the following three-step process:

1. Interpolate the output from each model to a common longitude/latitude

grid with 0.5° resolution.

2. Run the tracker on the interpolated grids. Keep in mind that the track files contain information from the smoothed data.

3. Use the storm center information from step 2 to search for the actual v_{max}, p_{min}, and r_{17}, r_{25}, r_{32} in the native model files, and overwrite the data in the track files with these new values.

Even after this process, the software tracked objects that human meteorologists would not identify as TCs, such as disorganized convective systems and heat lows over the deserts of Iran and central Asia. To reduce the number of falsely-identified objects as much as possible, the track files were quality-controlled using the following critera:

- drop all storms that form inland over Arabia and Iran,
- drop all storms with lifetimes under 48 h,
- drop all storms that never achieved a v_{max} of 7.5 m s^{-1},
- drop all records poleward of ±40° latitude (i.e., remove storms that become extratropical).

The IBTrACS data were quality-controlled using the same criteria to homogenize model data and observations.

3. Results

3.1 Number of Tropical Cyclones and Tracks

Fig. 1

Fig. 2

Meteorological services observed a global total of 24 TCs during the 40-day DYAMOND period, while the models simulated between 12–31 TCs, i.e., 50–140% of the observed value (Fig. 1). Most of the models simulated fewer TCs than observed; specifically, six of the nine models simulated less than 24 TCs (ARPEGE, FV3, ICON, IFS, MPAS, SAM; Figs. 1b,c,e,f,g,i), and only NICAM and UM simulated more TCs than observed (Figs. 1h,j). GEOS simulated exactly 24 TCs (Fig. 1d), however, given the limited sample size and the likelihood that a different tracker may have yielded slightly different numbers, we do not wish to emphasize the exact number of TCs each model produced.

According to the observations, the Western Pacific was the most active basin during the DYAMOND time period, followed by the Eastern Pacific, Atlantic, and Indian Ocean. All models agreed that the Western Pacific was going to be the most active basin , and the simulated tracks were generally oriented from south to north like in the observations (Fig. 1). A plausible reason for the track agreement is that all models were able to capture the large-scale steering flow over the Western Pacific. However, the models were not as successful in the other basins. For example, in the Eastern Pacific, all models except MPAS (Fig. 1g) simulated fewer TCs than observed, and there was less agreement between observed and simulated tracks. FV3 seems to have done best in terms of tracks in this basin (Fig. 1c). TC activity in the Atlantic proved to be particularly difficult to capture, and some models simulated a very active basin while others simulated a very quiet one. Specifically, NICAM produced 11 Atlantic TCs (Fig. 1h), whereas FV3 and IFS only produced one (Figs. 1c,f).

TC formation events during the DYAMOND period were not spread out uniformly over time but occurred in more or less well-defined periods (Fig. 2). The models simulated the temporal modulation of activity in rough agreement with the observations. For example, in the Western Pacific, most models correctly simulated a greater number of formation events before 22 August than after that date (Fig. 2a). In the Eastern Pacific, the models missed some of the formation events in early August, but they agreed with the observations on a second round of activity in late August/early September (Fig. 2b). In the Atlantic, about half of the models suggested a relatively active period in mid/late August, around the same time four formation events were observed (Fig. 2c). On the other hand, the models struggled with capturing the timing of TC formation in the Indian Ocean (Fig. 2d); however, with only two observed events, this basin is likely not representative.

At this point we can only speculate why the models were able to capture the temporal modulation of activity beyond the typical predictability limit of weather prediction, which is around two weeks. One possible reason is that the models were able to capture the modulating effect of intraseasonal variability as previously shown by Nakano et al. (2015). Another possible reason is that the pre-scribed sea-surface temperatures artificially impart longer predictability on the atmopshere.

Perhaps most importantly, Figure 2 demonstrates that no model suffered from a climate drift, that is, no model showed the number of TC formation events to unrealistically increase or decrease over the 40-day period. This highlights the quality of the DYAMOND models, which were not tuned for the experiment.

As a final remark, we note that UM produced three ensemble members in addition to the official 40-day DYAMOND run. The differences in TC numbers and tracks within that ensemble were as large as (or at times larger than) than inter-model differences (not shown). This indicates that more simulations and ensemble runs are needed to properly assess the predictive skill of each model beyond the broad statements made above.

3.2 Tropical Cyclone Intensity

Fig. 3

Fig. 4

Fig. 5

Fig. 6

Timeseries of v_{max} in Fig. 3 provide a broad overview of the intensity of the TCs and allow for a cursory model evaluation. Some biases are clearly evident; for example, ICON and SAM produced storms that were generally too weak (Figs. 3e,i), whereas ARPEGE produced a few storms that were much too strong. In fact, ARPEGE produced storms with unrealistically high v_{max} of >100 m s^{-1} (Fig. 3b), most likely because the evaporation coefficient was set to a wrong value (Stevens et al. 2019).

According to the observations, the TCs during the first two weeks of August remained relatively weak with only two storms reaching hurricane intensity (v_{max} $\geq$33 m s^{-1}; Fig. 3a). On the other hand, some of the TCs that formed in the second half of August became quite intense with four storms reaching major hurricane intensity (v_{max} $\geq$ 50 m s^{-1}). Most models had issues with capturing this pattern. Specifically, a number of models similated storms in the first half of August that were too intense (ARPEGE, GEOS, NICAM, UM; Figs. 3b,d,h,j). From all models, MPAS seems to have best captured the overall pattern (Fig. 3g).

To evaluate the models regarding intensity in more depth, we compared the observed and modeled frequency distributions of v_{max} (Fig. 4) and p_{min} (Fig. 5). We chose to compare frequency distributions instead of v_{max} and p_{min} errors, because the models did not simulate all observed TCs and not all simulated TCs were observed. We present the frequency distributions by way of *kernel density estimates* (Silverman 2018), because this method yields smooth curves that make a comparison easier. The kernel density estimates were implemented using the python seaborn library.

The observed v_{max} distribution has a broad primary peak centered near 20 m s^{-1}, a secondary peak near 50 m s^{-1}, and a fat tail towards higher values (Fig. 4). All models were able to produce this bi-modal distribution to some degree, but certain models deviated more from the observations than others. ICON and SAM deviated most dramatically: both models produced a narrow primary peak, mainly because they were not able to simulate high intensities (Figs. 4d,h). FV3 and GEOS shifted the secondary peak to higher values (Figs. 4b,c), whereas IFS and MPAS shifted it to lower values (Figs. 4e,f). ARPEGE produced a very broad distribution, partly related to its over-intensification issue (Fig. 4a). NICAM reproduced the observed distribution for $v_{max} > 25$ m s^{-1} better than the other models, but missed some of the weaker intensities with vmax < 20 m s^{-1} (Fig. 4g).

The observed p_{min} distribution has a well-defined primary peak around 1000 hPa, and a fat tail extending towards lower pressures with hint of a secondary maximum near 950 hPa (Fig. 5). All models were able to capture the general shape of the observed distribution, with MPAS and UM matching the observations best (Figs. 5f,i). Most of the other models produced storms that were too deep, although in different ways. In FV3, the distribution showed the same shape as the observation but shifted to deeper values (Figs. 5b); in IFS, the secondary maximum was much more pronounced than in the observations (Figs. 5f); and GEOS was somewhere in between FV3 and IFS (Figs. 5c). In ARPEGE and NICAM, some storms were much deeper than the observations, causing the tail to stretch too far to the left (Figs. 5a,g). SAM is unique in that the main peak was shifted to much higher values. We shall note here that SAM's p_{min} values are ambiguous, because SAM uses the anelastic equations and the quantity *pressure* can only be determined to within a function proportional to the base-state density field with arbitrary amplitude (Bannon et al. 2006).

Lastly, we evaluated the overall TC activity by means of *accumulated cyclone energy* (ACE), a quantity that estimates the wind energy produced by one or multiple TCs over their lifetime. It is computed according to ACE $= 10^{-4} \sum v_{max}^2$, where v_{max} is in units of knots (1 knot = 0.51 m s^{-1}). According to the observations, the ACE during the DYAMOND period was 169 (Fig. 6). Since the wind speed enters the ACE calculation as a squared value, ACE is quite sensitive to uncertainty in the analyzed v_{max} values. We therefore estimated a lower and upper bound by assuming that all observed v_{max} records have an error of ± 5 m s^{-1}, an estimate based on Torn and Snyder (2012) and Landsea and Franklin (2013). This assumption yielded a lower bound of 118 ACE units and an upper bound of 230 ACE units. Most models were within these uncertainty bounds or slightly above, indicating that the DYAMOND models produced realistic amounts of ACE, even without tuning. Only three models were outside the uncertainty bounds: GEOS overestimated ACE, whereas ICON and SAM produced less ACE than observed.

3.3 Tropical Cyclone Size

Fig. 7

Size is an important TC parameter because it correlates with the risk for storm surge, but it is often neglected and infrequently used for model validations. We examined the radius of gale-force winds (r_{17}) and present the median of all r_{17} records as our metric of choice (Fig. 7). Results for r_{25} and r_{32} were qualitatively similar (not shown), indicating that the results are not sensitive to a particular wind speed threshold. The observational error bars were computed by increasing/decreasing each r_{17} record by 50% (Landsea and Franklin 2013).

In general, the models overestimated TC size. TCs in ARPEGE, FV3, ICON, and NICAM were substantially larger than observed (Figs. 7a,b,d,g). In fact, ARPEGE and ICON produced very expansive wind fields, and their median r_{17} reached radially outward to 300 km (more than double the observations). In contrast, the median size of TCs in GEOS matched the observations remarkably well (Fig. 7c), and UM came in as a clear second (Fig. 7i). Storms in IFS and SAM were somewhat smaller than observed, but still within the uncertainty estimates (Figs. 7e,h). A common bias in the models was associated with the asymmetry of the wind field. Concretely, the observed r_{17} was largest in the northeast quadrant, but in FV3, ICON, MPAS, and NICAM, it was largest in the southeast quadrant (Figs. 7b,d,f,g). This result suggests that the models are deficient in their representation of TC structure; the prospect of which will be examined in the next section.

3.4 Tropical Cyclone Structure

Fig. 8

Fig. 9

Fig. 10

Fig. 11

Fig. 12

The TC wind-pressure relationship, i.e., the function that relates p_{min} to v_{max}, is often used to inform whether models simulate TC structure realistically. The DYAMOND models produced a variety of wind pressure relationships, with some models being closer to the observation than others (Fig. 8). FV3 and GEOS stand out for reproducing the observed relationship remarkably well (Fig. 8b, c). Most other models have a tendency to produce a relationship that drops off too fast, or in other words, for a given p_{min}, the v_{max} is too low. This behavior was most pronounced in ICON (Fig. 8d), and less noticeable in ARPEGE and MPAS (Fig. 8a,f). A possible explanation for this behavior will be discussed in section 4. SAM was unique and had an unrealistic wind-pressure relationship that bended upward (Fig. 8h). This phenomenon was not due to a single outlier but likely related to the the surface pressure field being an ambigous quantity in this model (see also section 3.2).

Since the 10-m winds in a TC and therefore v_{max} are strongly affected by the surface layer parameterization, we also investigated the relationship between p_{min} and 850-hPa v_{max}. The graphs were qualitatively similar to Fig. 8 (not shown), indicating that the wind-pressure relationships in Fig. 8 are not merely a product of each model's boundary layer and surface layer parameterizations, but stem from differences in the overall model implementation including the dynamical cores.

Snapshots of 10-m wind speed demonstrate the diversity of the models in simulating the surface wind field (Fig. 9). There were striking differences in eyewall shape, size, and symmetry, as well as in the radial extent of the wind field. Some models produced unrealistic wind fields, either too large and too strong (ARPEGE; Fig. 9a), or too faint and with peculiar waviness (SAM; Fig. 9h). The wind fields of FV3, GEOS, and MPAS were arguably most similar to that of a canonical intense TC, with a distinct eyewall that contained multiple convective- and mesoscale asymmetries (Figs. 9b,c,f).

The ICON example was unique in that it did not reveal a distinct eyewall with sharp gardients; its wind field was rather diffuse and spread out over a large area (Fig. 9d). In contrast, the IFS example was a very small TC with a radially constrained wind field (Fig. 9e). The NICAM example, Fig. 9g, had an even larger hurricane-force (wind speed $\geq$33 m s^{-1}) wind field than ICON, but it also had a distinct eyeall like most other models—albeit somewhat smoother than the eyewalls in FV3, GEOS, and MPAS. The wind field from the UM example exhibited the smoothest structure, the widest eyewall, and the clearest imprint of the model mesh—all consistent with UM being the model with the lowest resolution (Fig. 9i).

A closer look at the kinematic structure of the modeled TCs was achieved by creating composites of the azimuthally-averaged circulation (Fig. 10). Each model's composite includes the individual cases where $v_{max} \geq 33$ m s^{-1}. Broadly speaking, all models produced a typical kinematic structure, that is, a well-defined *primary circulation* with a tangential wind maximum in the lower troposphere near the storm center, and a well-defined *secondary circulation* manifested by strong radial inflow in the boundary layer, rising motion in the eyewall region, and radial outflow in the mid- to upper troposphere. Despite the overall agreement, there were noteworthy differences between the models, which will be discussed next. Note that we will assume that the inter-model structure differences are due to model formulation and not due the varying intensity of the composite storms.

The differences in the overall tangential wind structure can be elucidated by comparing the size of the radius of maximum tangential wind, the compactness of the wind maximum (specifically, the radial extent of the 35 m s^{-1} isotach), and the decay of the tangential wind in the radial and vertical direction. The composite storms had radii of maximum tangential wind roughly between 30–70 km, with ARPEGE and IFS on the lower end (Figs. 10a,e) and ICON on the upper end (Fig. 10d). In FV3 and MPAS, the wind maximum was comparatively narrow and confined, and the radial extent of the 35 m s^{-1} isotach was less than 20 km (Figs. 10b,f). On the other hand, in ICON and NICAM, the wind maximum was rather broad, and the radial extent of the 35 m s^{-1} isotach was greater than 50 km (Figs. 10e,g). Differences in the radial and vertical decay rates mirror the previous discussion of storm size, that is, models in which the tangential wind decayed more slowly, such as in ICON and NICAM, were the ones that produced comparatively larger storms.

Given the lack of an equivalent observational dataset, it is difficult to assess what model produced a particularly realistic tangential wind structure. The observational composites of Gao et al. (2019, their Fig. 5c) and Komaromi and Doyle (2017, their Fig. 7a) at least suggests that no model produced a particularly unrealistic structure.

As for the vertical motion, ARPEGE and IFS had the steepest eyewall slopes (Figs. 10a,e). The other extreme was UM, which had the most pronounced eyewall tilt (Fig. 10i). In ICON and NICAM, the eyewall updraft was spread out and diffuse (Figs. 10d,g), but in IFS and MPAS it was relatively narrow and confined (Figs. 10e,f). Besides these differences in the eyewall region, there were differences in the rainband region, too. Specifically, the vertical motion between r = 100–250 km was noticeably stronger in ICON, MPAS, and NICAM than in GEOS, IFS, and SAM (Figs. 10d,f,g versus Figs. 10c, e,h). This difference may be a reflection of more or stronger rainbands in the former models.

Again, it is difficult to say which models produced a particularly realistic structure because no equivalent observational dataset exists for the TCs observed during the DYAMOND period. Stern and Nolan (2009) showed that the slope of the eyewall depends on the size of the radius of maximum wind, which would explain why the eyewall updraft in IFS has a steeper slope than in IFS, but it cannot explain the differences between models with similarly sized radii of maximum wind, such as MPAS and UM.

The upper-tropospheric outflow also differed between the models, especially with regard to the altitude of the outflow maximum and the depth of the outflow layer. For instance, the outflow was comparatively deep in FV3 (Fig. 10b) and comparatively shallow in IFS (Fig. 10e). In ARPEGE and ICON, the outflow maximum occurred at a height of 15 km (Figs. 10a,d), but in most of the other models, it occurred mostly below 15 km.

One particularly noteworthy feature, produced somewhat more prominently by FV3, GEOS, and IFS, is the descending flow above the outflow layer that merges with the ascending outflow from below (Figs. 10b,c,e). We are not aware of either observational or modeling studies that show such a feature in TCs; to the contrary, there is reasonable evidence to suggest that at least in intense TCs, it may be common to have a shallow layer of weak inflow atop the upper-level outflow layer (e.g., Kieu et al. 2016; Komaromi and Doyle 2017; Heng et al. 2017; Duran and Molinari 2018).

Inter-model differences in the boundary layer inflow were mostly in the form of variations of inflow layer depth and strength (Fig. 11). Specifically, IFS and SAM produced comparatively shallow inflow layers that did not extend much above 1 km height (Figs. 11e,h). In GEOS and ICON, the inflow layer had a maximum depth of 1.5 km (Figs. 11c,d), and in the other models, its maximum depth extended slightly above 1.5 km. The observational composite of Zhang et al. (2011, their Fig. 5b) shows that the inflow layer depth increases from 900 m at the radius of maximum wind to 1.5 km roughly 200 km from the center, which is in broad agreement with most of the models.

From basic TC dynamics one would expect that the inflow strength correlate with the average intensity of the TCs simulated by the models. However, this was not the case. For example, ICON, which simulated mostly weak TCs, produced stronger inflow than FV3, MPAS, and NICAM, which simulated much stronger TCs (Fig. 11d vs. Figs. 11b,f,g). In fact, with inflow magnitudes of 9 m s^{-1}, the inflow in FV3, MPAS, and NICAM was relatively weak not only compared to the other models, but also compared to observations, which show an inflow magnitude of 20 m s^{-1} (Zhang et al. 2011).

Besides teh kinematic structure, we also explored the thermodynamic TC structure in our set of global storm-resolving simulations. To this end, we examined the TC warm core, here represented by the temperature anomaly with respect to the mean temperature between r=300–700 km (Fig. 12). All models produced a warm core, and all models agreed on its general structure (expansive in the upper levels, radially confined below). Differences emerged mostly in the vertical structure of the warming inside the TC eye, and in the upper and lower level temperature anomalies outside the eye.

Most models agreed that the warm anomaly peaks at a height of just under 10 km. More pronounced differences between the models appeared in the vertical structure of the warm core, which ranged from a single, vertically confined maximum in FV3 and GEOS (Figs. 12b,c), to an extended vertical column in NICAM (Fig. 12g), to a clear double maximum of anomalously warm air in UM (Fig. 12i). The other models fell somewhere in between these three distinct cases. Most observational studies indicate that the warm core is maximized in the upper troposphere (Frank 1977; Brammer and Thorncroft 2017; Komaromi and Doyle 2017), in agreement with most of the DYAMOND models. However, Stern and Nolan (2012) claimed that the maximum warming should be between 4–8 km, with a potential secondary maximum at higher altitudes. Kieu et al. (2016) also claimed that a double-warm core structure is the norm rather than the exception. According to those studies, UM had a particularly realistic thermodynamic structure, even though it was an outlier among the DYAMOND models.

Compared to the model differences in terms of the warm core, the differences above the outflow layer were equally if not more striking. Above 15-km height, the models did not even agree on the sign of the temperature anomaly. In particular, IFS and ARPEGE produced a strong cool anomaly (<-3 K; incidentally, IFS and ARPEGE were the only spectral models), whereas NICAM, SAM, and UM produced a warm anomaly. FV3, GEOS, ICON, and MPAS were somewhere in between the extremes and produced a weak cool anomaly (>-1 K). Observational composites generally show a weak cold anomaly above the outflow layer (Frank 1977; Komaromi and Doyle 2017), although instantaneous snapshots of intense TCs may also show strong cold anomalies (Komaromi and Doyle 2017).

Temperature differences were also found in the boundary layer, although less dramatic: NICAM was anomalously cool (Fig. 12g), and IFS was anomalously warm (Fig. 12e). The other models had weak cool anomalies or no clear signal. Note that IFS and NICAM were polar opposites of each other (NICAM: warm in the upper levels, cool in the lower levels, IFS: vice versa).

3.5 Sensitivity of Tropical Cyclone Formation and Intensity to Model Resolution and Parameterized Deep Convection

Fig. 13

Fig. 14

In addition to the primary high-resolution simulation, some DYAMOND models produced sensitivity runs with lower resolution. For example, ICON produced six simulations with mesh spacings of 2.5, 5, 10, 20, 40, and 80 km, all **without** parameterized convection (ICON no-conv), and an additional three simulations with mesh spacings of 20, 40, and 80 km **with** parameterized convection (ICON conv). These nine simulations provided an opportunity to investigate the sensitivity to model resolution and parameterized convection in a controlled way (Fig. 13, Fig. 14) .

As for sensitivity to resolution, there was a clear inverse relationship and the number of simulated TCs **increased** when resolution was **decreased** (Fig. 13, left column). Concretely, the highest resolution run produced the fewest TCs (15; Fig. 13a), and the lowest resolution run produced the most TCs (50; Fig. 13h). In the simulations with intermediate resolution, the number of TCs was relatively constant (around 20). The sensitivity to resolution seemed to be basin dependent. In the Atlantic and Eastern Pacific, the 80-km ICON produced five to six times as many TCs as the 2.5-km ICON (Figs. 13a,h), but in the Western Pacific, the 80-km ICON produced only two times as many TCs as the 2.5-km ICON. In the Indian Ocean, the number of events seemed to be insensitive to resolution, and each run produced either one or two TCs.

As for sensitivity to parameterized convection, the model produced dramatically fewer TCs once the parameterization was turned on (Fig. 13, left vs. right column). This effect was most pronounced at lower resolution. Specifically, the number of TCs dropped from 23 to 17 in the 20-km runs (Figs. 13d,e), from 21 to 14 in the 40-km runs (Figs. 13f,g), and from 50 to a mere 9 in the 80-km runs (Figs. 13h,i).

The runs with parameterized convection also featured substantially lower ACE (Fig. 14). Again, the effect was most dramatic at lower resolution, but even for an intermediate resolution of 20 km, the ACE was reduced by 65%. This result suggests that convection parameterization did not just reduce the number of TCs, but it also made them weaker and their lifetime shorter.

Interestingly, the ICON no-conv runs produced more or less the same amount of ACE at all resolutions (Fig. 14). Evidently, the lack of intense storms in the lower-resolution runs was compensated by a larger number of weak storms. An interesting follow-up question would be to investigate whether this compensation was pure luck or whether the amount of background available potential energy that is converted to kinetic energy by TCs is a resolution-independent quantity, such as mean precipitation (Hohenegger et al. 2020).

4. Discussion

Fig. 15

One of the drawbacks of global storm-resolving models is their immense computational cost, which poses questions about cost versus benefit. One may, for example, postulate that regional high-resolution models suffice for TC prediction. Although a practical alternative, regional models have disadvantages such as determining the ideal domain size and placement for a regional domain. More importantly, regional domains require lateral boundary conditions, which have "serious negative effects" (Warner et al. 1997). One of those effects is that errors creep in through the boundaries and render longer-range forecasts less skillful than those made by global models. Putting it slightly differently, regional models are very dependent on the global model forcing being "good enough".

One may also follow Manganello et al. (2012) and argue that hydrostatic models with mesh spacings of 10 km and parameterized convection are sufficient for producing realistic TCs. Nonetheless, mesh spacings of <5 km are still required for realistically simulating v_{max} and the dynamic processes in the TC inner core (e.g., Chen et al. 2007; Gentry and Lackmann 2010; Judt and Chen 2010; Gopalakrishnan et al. 2012; Davis 2018). Observations and numerical models indicate that such processes are important for rapid intensification (e.g., Miyamoto and Takemi 2015; Guimond et al. 2016; Judt and Chen 2016). In fact, a case study by Fox and Judt (2018) suggested that simulating extreme cases of rapid intensification requires ≤1 km horizontal grid spacing. Since extreme storms are highly disruptive to society, being able to reliably predict or project intense TCs has great value.

As a potential easy target for bias reduction in the models, we examined whether models with similar biases used similar parameterization schemes. For example, we investigated whether the models with a TKE-like boundary layer parameterization produced similar intensity biases versus models that used a diagnostic eddy diffusivity. However, no such relationships were found. In the end, there are variety of reasons for the model diversity, including but not limited to: cloud microphysics, boundary layer processes, and the dynamical cores (with differences in effective resolutions).

In agreement with other studies, this paper also demonstrates that high resolution is necessary yet not sufficient to capture the v_{max} of TCs. For example, ICON was tied with ARPEGE for highest resolution (2.5 km), yet ICON struggled to produce intense TCs while ARPEGE produced unrealistically strong TCs. These intensity biases are likely a consequence of the respective model's surface flux formulation, as demonstrated by Fig. 15, which shows the surface fluxes of momentum and latent heat over an area 300×300 km centered on the strongest TC in each model. The drag in ICON increased much faster with wind speed than in ARPEGE (Fig. 15a), which means that there was a comparatively stronger "break" on the surface wind in ICON. ICON also had significantly weaker latent heat fluxes for a given wind speed, providing less amount of "fuel" (Fig. 15b).

The monotonically increasing momentum flux in Fig. 15a also indicates that the models did not account for the saturation of the drag at wind speeds above 25 m s^{-1} (e.g., Powell et al. 2003; Donelan 2004; Chen et al. 2013; Curcic and Haus 2020). This shortcoming was found in other models as well (not shown), and it may be the reason why the wind-pressure relationship in several models deviated from observations at higher winds (Fig. 8). In fact, the wind-pressure relationship in IFS seems to improve when drag is computed in a more realistic three-way coupled atmosphere-wave-ocean model (Magnusson et al. 2019).

Lastly, there is much evidence that the storm count (and storm-count-related model biases) are sensitive to the tracker and to the model formulation/resolution (Roberts et al. 2020; Vanniere et al. 2020). This can be an issue when comparing models as weak TCs might be over- or under-detected depending on the threshold used. In the end, only further studies can speak to the robustness of the results presented in this paper.

5. Summary and Conclusions

We evaluated nine global storm-resolving models that participated in the DYAMOND initiative (Stevens et al. 2019) in their ability to simulate TCs. Specifically, we validated and compared the number of TCs each model produced, their tracks, intensity, size, and structure. With mesh spacings between 2.5–7.8 km, the DYAMOND models are the highest-resolution global models that have so far been analyzed for this purpose.

The results suggest that global storm-resolving models are able to simulate the structure and intensity of TCs more realistically than previous generations of global models. However, we found that TCs are strongly affected by model formulation, and essentially all models had biases. We found that no model did best in all regards, although some models did, generally speaking, better than others. For instance, GEOS produced the observed number of TCs, captured TC size better than any other model, and produced a realistic wind-pressure relationship. But GEOS also produced too many strong storms and had the largest ACE bias of all models (it is unclear if ocean coupling would reduce this bias). Other models that did generally well were FV3, MPAS, and UM.

On the other hand, ICON, IFS, and SAM had some issues with size, structure, and intensity. For example, ICON and SAM produced storms that were too weak. ICON, IFS, and SAM were also not able to capture the wind-pressure relationship as realistically as GEOS, FV3, and MPAS, pointing to deficiencies in their numerical formulations. We also found that parameterized convection strongly reduces the number and intensity of TCs in comparison to simulations without convection parameterization (at least for simulations with a mesh spacing of >20 km). This sensitivity highlights the problems and ambiguities that come with parameterizing deep convection.

In a nutshell, we believe that the ability to realistically simulate TCs in global models is critical for weather and climate prediction. This study demonstrates that global-storm resolving models are an optimal tool to advance TC prediction; however, they need to be improved to unleash their full potential. Surface layer, pbl are targets for improvements.

Acknowledgements

This material is based upon work supported by the National Center for Atmospheric Research, which is a major facility sponsored by the National Science Foundation under Cooperative Agreement No. 1852977. Support by the Centre of Excellence ESiWACE is acknowledged. ESiWACE has received funding from the European Unions Horizon 2020 research and innovation programme under grant agreement numbers 675191 and 823988. The authors thank the German Climate Computing Center for hosting, providing access to and supporting at evaluating the DYAMOND data sets. We acknowledge high-performance computing support from Cheyenne (doi:10.5065/D6RX99HX) provided by NCAR's Computational and Information Systems Laboratory, sponsored by the National Science Foundation. RS, MS, MN and CK were supported by the FLAGSHIP2020 within the priority study4 (Advancement of meteorological and global environmental predictions utilizing observational "Big Data") and the Integrated Research Program for Advancing Climate Models (TOUGOU) Grant Number JPMXD0717935457 from the Ministry of Education, Culture, Sports, Science, and Technology of Japan. The NICAM simulation was performed on the Earth Simulator of the Japan Agency for Marine-Earth Science and Technology. MR, PLV and BV acknowledge funding from the EU H2020 PRIMAVERA project under Grant Agreement no. 641727. The authors would also like to thank David Ahijvevych for his assitance with the GFDL tracker, and Dan Stern, Will Komaromi, and Kevin Hodges for valuable comments. The comments from XXX reviewers helped improving the manuscript.

References

Bannon, P. R., J. M. Chagnon, and R. P. James, 2006: Mass conservation and the anelastic approximation. *Monthly Weather Review*, **134(10)**, 2989–3005.

Bengtsson, L., K. I. Hodges, M. Esch, N. Keenlyside, L. Kornblueh, J.-J. Luo, and T. Yamagata, 2007: How may tropical cyclones change in a warmer climate? *Tellus A: Dynamic Meteorology and Oceanography*, **59(4)**, 539–561.

Biswas, M. K., D. Stark, and L. Carson, 2018: *GFDL Vortex Tracker Users' Guide V3.9a*. National Center for Atmospheric Research, Developmental Testbed Center.

Brammer, A., and C. D. Thorncroft, 2017: Evaluation of reanalysis tropical cyclone structure with global hawk 1 dropsonde observations.

Camargo, S. J., A. G. Barnston, and S. E. Zebiak, 2005: A statistical assessment of tropical cyclone activity in atmospheric general circulation models. *Tellus A: Dynamic Meteorology and Oceanography*, **57(4)**, 589–604.

Chen, S. S., J. F. Price, W. Zhao, M. A. Donelan, and E. J. Walsh, 2007: The CBLAST-hurricane program and the next-generation fully coupled atmosphere–wave–ocean models for hurricane research and prediction. *Bulletin of the American Meteorological Society*, **88(3)**, 311–318.

Chen, S. S., W. Zhao, M. A. Donelan, and H. L. Tolman, 2013: Directional wind–wave coupling in fully coupled atmosphere–wave–ocean models: Results from CBLAST-hurricane. *Journal of the Atmospheric Sciences*, **70(10)**, 3198–3215.

Curcic, M., and B. K. Haus, 2020: Revised estimates of ocean surface drag in strong winds. *Geophysical Research Letters*, **47(10)**.

Davis, C., W. Wang, S. S. Chen, Y. Chen, K. Corbosiero, M. DeMaria, J. Dudhia, G. Holland, J. Klemp, J. Michalakes, H. Reeves, R. Rotunno, C. Snyder, and Q. Xiao, 2008: Prediction of landfalling hurricanes with the advanced hurricane WRF model. *Monthly Weather Review*, **136(6)**, 1990–2005.

Davis, C. A., 2018: Resolving tropical cyclone intensity in models. *Geophysical Research Letters*, **45(4)**, 2082–2087.

DeMaria, M., C. R. Sampson, J. A. Knaff, and K. D. Musgrave, 2014: Is tropical cyclone intensity guidance improving? *Bulletin of the American Meteorological Society*, **95(3)**, 387–398.

Donelan, M. A., 2004: On the limiting aerodynamic roughness of the ocean in very strong winds. *Geophysical Research Letters*, **31(18)**.

Duran, P., and J. Molinari, 2018: Dramatic inner-core tropopause variability during the rapid intensification of hurricane patricia (2015). *Monthly Weather Review*, **146(1)**, 119–134.

Fox, K. R., and F. Judt, 2018: A numerical study on the extreme intensification of hurricane patricia (2015). *Weather and Forecasting*, **33(4)**, 989–999.

Frank, W. M., 1977: The structure and energetics of the tropical cyclone i. storm structure. *Monthly Weather Review*, **105(9)**, 1119–1135.

Fudeyasu, H., Y. Wang, M. Satoh, T. Nasuno, H. Miura, and W. Yanase, 2008: Global cloud-system-resolving model NICAM successfully simulated the lifecycles of two real tropical cyclones. *Geophysical Research Letters*, **35(22)**.

Gao, K., L. Harris, J.-H. Chen, S.-J. Lin, and A. Hazelton, 2019: Improving AGCM hurricane structure with two-way nesting. *Journal of Advances in Modeling Earth Systems*, **11(1)**, 278–292.

Gentry, M. S., and G. M. Lackmann, 2010: Sensitivity of simulated tropical cyclone structure and intensity to horizontal resolution. *Monthly Weather Review*, **138(3)**, 688–704.

Gopalakrishnan, S. G., S. Goldenberg, T. Quirino, X. Zhang, xf Marks, K.-S. Yeh, R. Atlas, and V. Tallapragada, 2012: Toward improving high-resolution numerical hurricane forecasting: Influence of model horizontal grid resolution, initialization, and physics. *Weather and Forecasting*, **27(3)**, 647–666.

Green, B. W., and F. Zhang, 2013: Impacts of air–sea flux parameterizations on the intensity and structure of tropical cyclones. *Monthly Weather Review*, **141(7)**, 2308–2324.

Guimond, S. R., G. M. Heymsfield, P. D. Reasor, and A. C. Didlake, 2016: The rapid intensification of hurricane karl (2010): New remote sensing observations of convective bursts from the global hawk platform. *Journal of the Atmospheric Sciences*, **73(9)**, 3617–3639.

Hamill, T. M., J. S. Whitaker, M. Fiorino, and S. G. Benjamin, 2011: Global ensemble predictions of 2009's tropical cyclones initialized with an ensemble kalman filter. *Monthly Weather Review*, **139(2)**, 668–688.

Harper, B. A., J. D. Kepert, and J. D. Ginger, 2008: , Guidelines for converting between various wind averaging periods in tropical cyclone conditions, world meteorological organization. Technical report, World Meteorological Organization.

Heng, J., Y. Wang, and W. Zhou, 2017: Revisiting the balanced and unbalanced aspects of tropical cyclone intensification. *Journal of the Atmospheric Sciences*, **74(8)**, 2575–2591.

Hodges, K. I., and N. P. Klingaman, 2019: Prediction errors of tropical cyclones in the western north pacific in the met office global forecast model. *Weather and Forecasting*, **34(5)**, 1189–1209.

Hohenegger, C., L. Kornblueh, D. Klocke, T. Becker, G. Cioni, J. F. Engels, U. Schulzweida, and B. Stevens, 2020: Climate statistics in global simulations of the atmosphere, from 80 to 2.5 km grid spacing. *Journal of the Meteorological Society of Japan. Ser. II*, **98(1)**, 73–91.

Judt, F., and S. S. Chen, 2010: Convectively generated potential vorticity in rainbands and formation of the secondary eyewall in hurricane rita of 2005. *Journal of the Atmospheric Sciences*, **67(11)**, 3581–3599.

Judt, F., and S. S. Chen, 2016: Predictability and dynamics of tropical cyclone rapid intensification deduced from high-resolution stochastic ensembles. *Monthly Weather Review*, **144(11)**, 4395–4420.

Kanada, S., A. Wada, M. Nakano, and T. Kato, 2012: Effect of planetary boundary layer schemes on the development of intense tropical cyclones using a cloud-resolving model. *Journal of Geophysical Research: Atmospheres*, **117(D3)**, n/a–n/a.

Kepert, J. D., 2012: Choosing a boundary layer parameterization for tropical cyclone modeling. *Monthly Weather Review*, **140(5)**, 1427–1445.

Kieu, C., V. Tallapragada, D.-L. Zhang, and Z. Moon, 2016: On the development of double warm-core structures in intense tropical cyclones. *Journal of the Atmospheric Sciences*, **73(11)**, 4487–4506.

Knapp, K. R., H. J. Diamond, J. P. Kossin, M. C. Kruk, and C. J. Schreck, 2018: International best track archive for climate stewardship (ibtracs) project, version 4.

Knapp, K. R., M. C. Kruk, D. H. Levinson, H. J. Diamond, and C. J. Neumann, 2010: The international best track archive for climate stewardship (IBTrACS). *Bulletin of the American Meteorological Society*, **91(3)**, 363–376.

Komaromi, W. A., and J. D. Doyle, 2017: Tropical cyclone outflow and warm core structure as revealed by HS3 dropsonde data. *Monthly Weather Review*, **145(4)**, 1339–1359.

Landsea, C. W., and J. L. Franklin, 2013: Atlantic hurricane database uncertainty and presentation of a new database format. *Monthly Weather Review*, **141(10)**, 3576–3592.

Lee, C.-Y., and S. S. Chen, 2014: Stable boundary layer and its impact on tropical cyclone structure in a coupled atmosphere–ocean model. *Monthly Weather Review*, **142(5)**, 1927–1944.

Magnusson, L., J.-R. Bidlot, M. Bonavita, A. R. Brown, P. A. Browne, G. D. Chiara, M. Dahoui, S. T. K. Lang, T. McNally, K. S. Mogensen, F. Pappenberger, F. Prates, F. Rabier, D. S. Richardson, F. Vitart, and S. Malardel, 2019: ECMWF activities for improved hurricane forecasts. *Bulletin of the American Meteorological Society*, **100(3)**, 445–458.

Manganello, J. V., K. I. Hodges, J. L. Kinter, B. A. Cash, L. Marx, T. Jung, D. Achuthavarier, J. M. Adams, E. L. Altshuler, B. Huang, E. K. Jin, C. Stan, P. Towers, and N. Wedi, 2012: Tropical cyclone climatology in a 10-km global atmospheric GCM: Toward weather-resolving climate modeling. *Journal of Climate*, **25(11)**, 3867–3893.

Marchok, T. P., 2002: How the ncep tropical cyclone tracker works. In *AMS Conference on Hurricanes and Tropical Meteorology, San Diego, CA, P1.13*, American Meteorological Society.

Miyamoto, Y., and T. Takemi, 2015: A triggering mechanism for rapid intensification of tropical cyclones. *Journal of the Atmospheric Sciences*, **72(7)**, 2666–2681.

Mogensen, K. S., L. Magnusson, and J.-R. Bidlot, 2017: Tropical cyclone sensitivity to ocean coupling in the ECMWF coupled model. *Journal of Geophysical Research: Oceans*, **122(5)**, 4392–4412.

Nakano, M., M. Sawada, T. Nasuno, and M. Satoh, 2015: Intraseasonal variability and tropical cyclogenesis in the western north pacific simulated by a global nonhydrostatic atmospheric model. *Geophysical Research Letters*, **42(2)**, 565–571.

Nakano, M., A. Wada, M. Sawada, H. Yoshimura, R. Onishi, S. Kawahara, W. Sasaki, T. Nasuno, M. Yamaguchi, T. Iriguchi, M. Sugi, and Y. Takeuchi, 2017: Global 7-km mesh nonhydrostatic model intercomparison project for improving TYphoon forecast (TYMIP-g7): experimental design and preliminary results. *Geoscientific Model Development*, **10(3)**, 1363–1381.

Powell, M. D., P. J. Vickery, and T. A. Reinhold, 2003: Reduced drag coefficient for high wind speeds in tropical cyclones. *Nature*, **422(6929)**, 279–283.

Roberts, M. J., J. Camp, J. Seddon, P. L. Vidale, K. Hodges, B. Vanniere, J. Mecking, R. Haarsma, A. Bellucci, E. Scoccimarro, L.-P. Caron, F. Chauvin, L. Terray, S. Valcke, M.-P. Moine, D. Putrasahan, C. Roberts, R. Senan, C. Zarzycki, and P. Ullrich, 2020: Impact of model resolution on tropical cyclone simulation using the HighResMIP–PRIMAVERA multimodel ensemble. *Journal of Climate*, **33(7)**, 2557–2583.

Satoh, M., B. Stevens, F. Judt, M. Khairoutdinov, S.-J. Lin, W. M. Putman, and P. Düben, 2019: Global cloud-resolving models. *Current Climate Change Reports*, **5(3)**, 172–184.

Silverman, B., 2018: *Density Estimation for Statistics and Data Analysis*. Routledge.

Stern, D. P., and D. S. Nolan, 2009: Reexamining the vertical structure of tangential winds in tropical cyclones: Observations and theory. *Journal of the Atmospheric Sciences*, **66(12)**, 3579–3600.

Stern, D. P., and D. S. Nolan, 2012: On the height of the warm core in tropical cyclones. *Journal of the Atmospheric Sciences*, **69(5)**, 1657–1680.

Stevens, B., M. Satoh, L. Auger, J. Biercamp, C. S. Bretherton, X. Chen, P. Düben, F. Judt, M. Khairoutdinov, D. Klocke, C. Kodama,

L. Kornblueh, S.-J. Lin, P. Neumann, W. M. Putman, N. Röber, R. Shibuya, B. Vanniere, P. L. Vidale, N. Wedi, and L. Zhou, 2019: DYAMOND: the DYnamics of the atmospheric general circulation modeled on non-hydrostatic domains. *Progress in Earth and Planetary Science*, **6(1)**.

Torn, R. D., and C. Snyder, 2012: Uncertainty of tropical cyclone best-track information. *Weather and Forecasting*, **27(3)**, 715–729.

Vanniere, B., M. J. Roberts, P. L. Vidale, K. I. Hodges, M.-E. Demory, L.-P. Caron, E. Scoccimarro, L. Taurent, and R. Senan, 2020: The moisture budget of tropical cyclones in highresmip models : large-scale environmental balance and sensitivity to horizontal resolution. *submitted to Journal of Climate*.

Warner, T. T., R. A. Peterson, and R. E. Treadon, 1997: A tutorial on lateral boundary conditions as a basic and potentially serious limitation to regional numerical weather prediction. *Bulletin of the American Meteorological Society*, **78(11)**, 2599–2617.

Zeng, Z., Y. Wang, Y. Duan, L. Chen, and Z. Gao, 2010: On sea surface roughness parameterization and its effect on tropical cyclone structure and intensity. *Advances in Atmospheric Sciences*, **27(2)**, 337–355.

Zhang, J. A., D. S. Nolan, R. F. Rogers, and V. Tallapragada, 2015: Evaluating the impact of improvements in the boundary layer parameterization on hurricane intensity and structure forecasts in HWRF. *Monthly Weather Review*, **143(8)**, 3136–3155.

Zhang, J. A., R. F. Rogers, D. S. Nolan, and F. D. Marks, 2011: On the characteristic height scales of the hurricane boundary layer. *Monthly Weather Review*, **139(8)**, 2523–2535.

Zhou, L., S.-J. Lin, J.-H. Chen, L. M. Harris, X. Chen, and S. L. Rees, 2019: Toward convective-scale prediction within the next generation global prediction system. *Bulletin of the American Meteorological Society*, **100(7)**, 1225–1243.

List of Figures

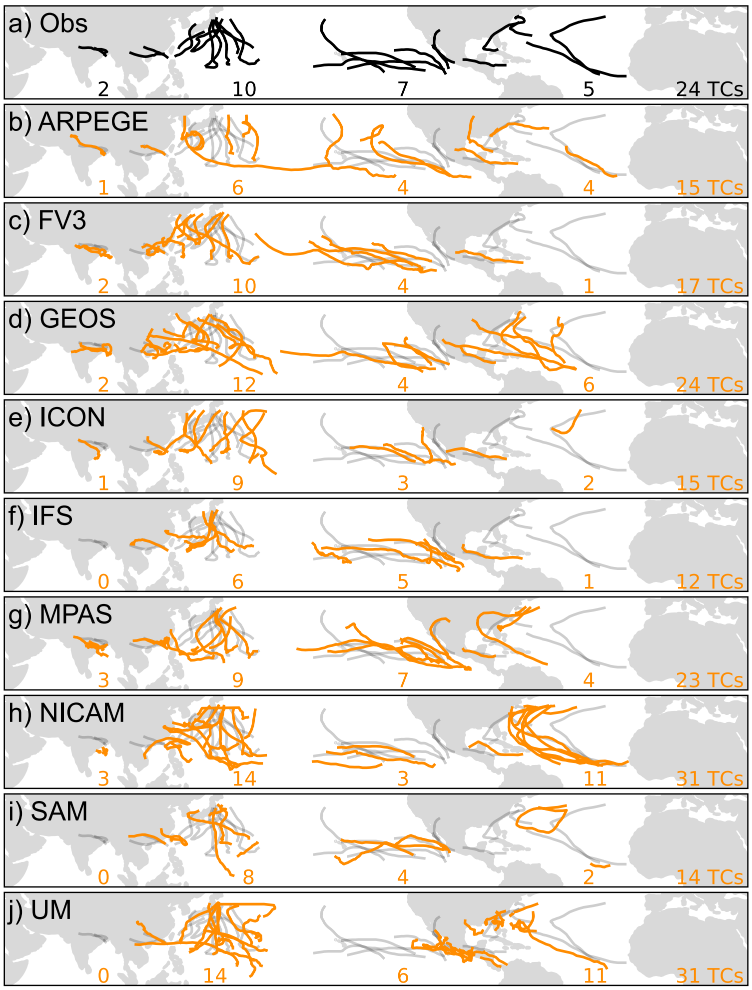

Fig. 1. TC tracks and numbers from observations (black/grey) and models (orange) for the DYAMOND period (1 Aug–10 Sep 2016). Numbers are given for each basin (Indian Ocean, Western Pacific, Eastern Pacific, Atlantic); the global total number of TCs is shown in the lower right.

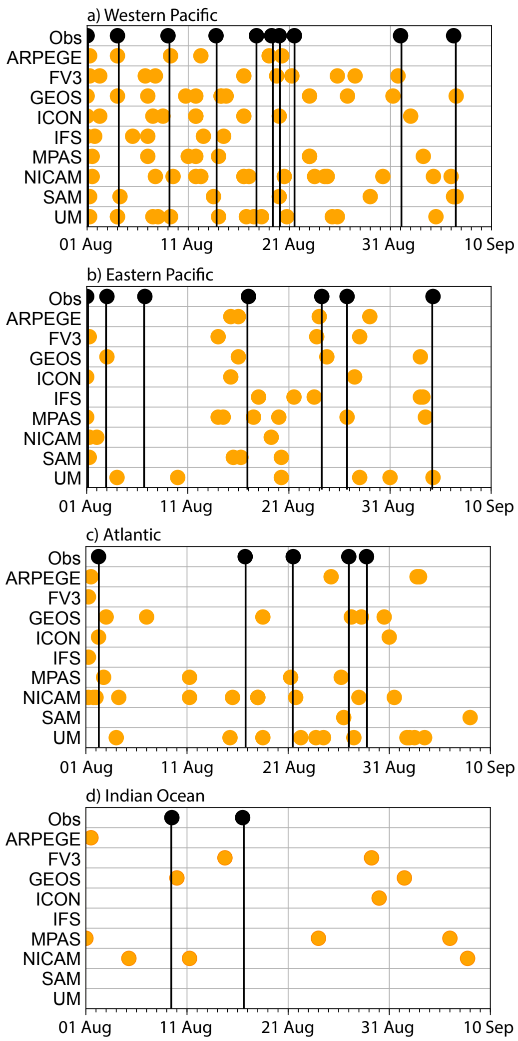

Fig. 2. Timeseries of TC formation events in the Western Pacific (a), Eastern Pacific (b), Atlantic (c), and Indian Ocean (d) from observations (black) and models (orange).

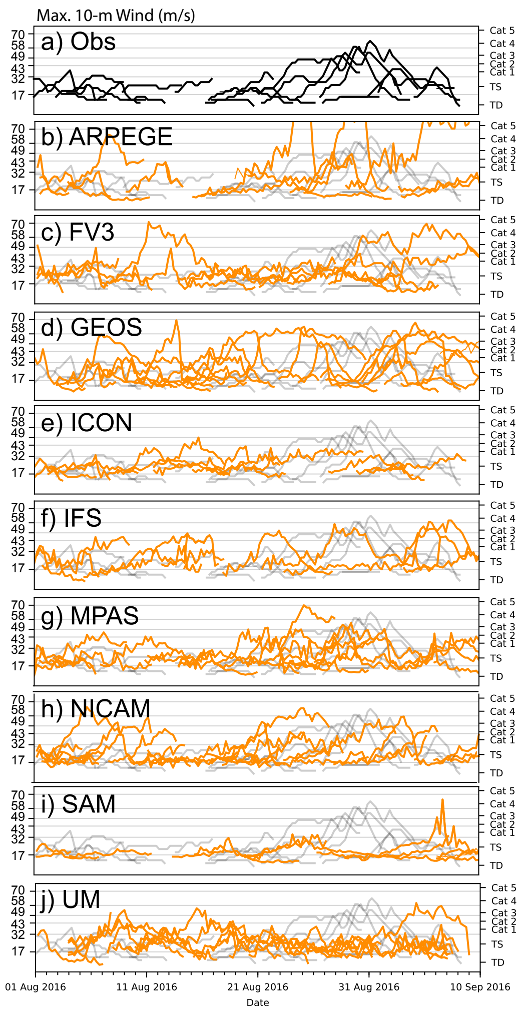

Fig. 3. Timeseries of maximum surface wind speed (v_{max}) for each TC from observations (black, grey) and models (orange).

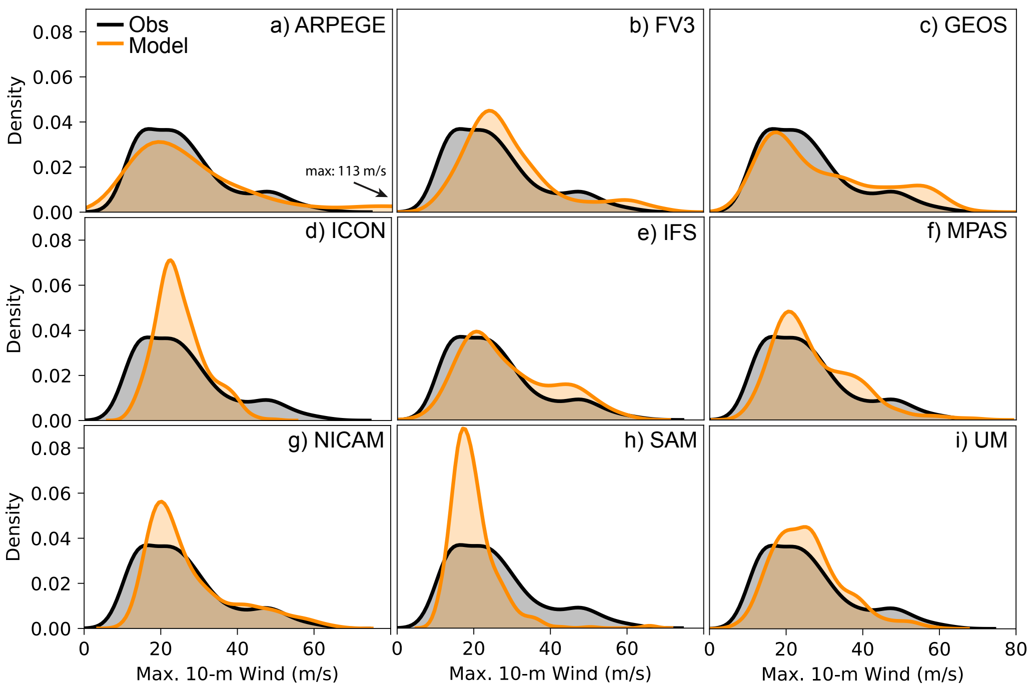

Fig. 4. Kernel density estimates of maximum wind speed from observations (black) and models (orange).

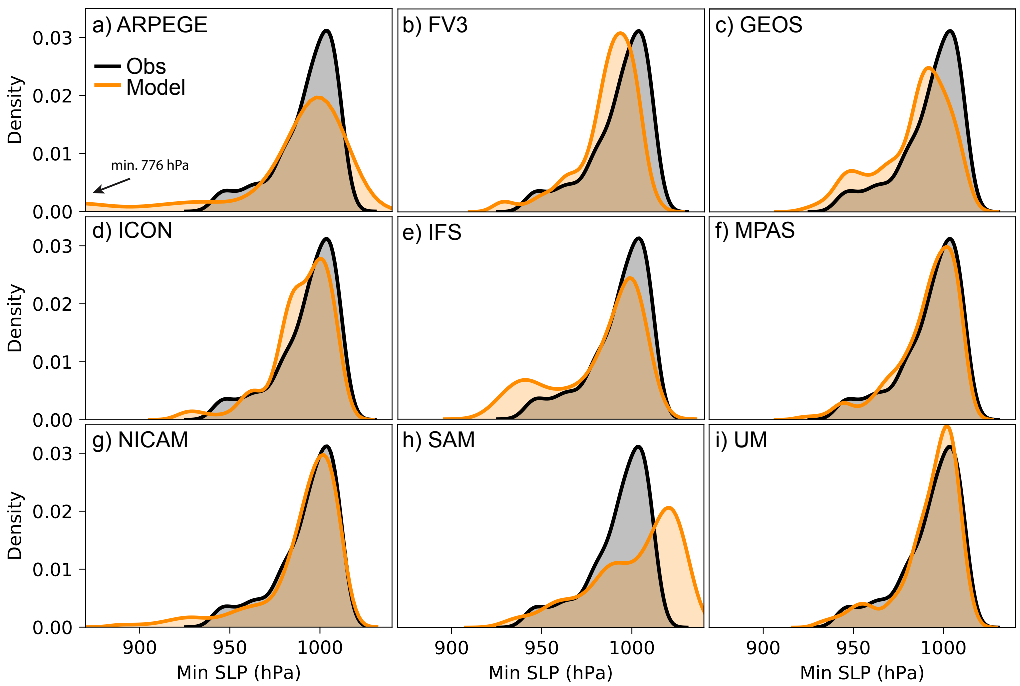

Fig. 5. Kernel density estimates of minimum sea-level pressure from observations (black) and models (orange).

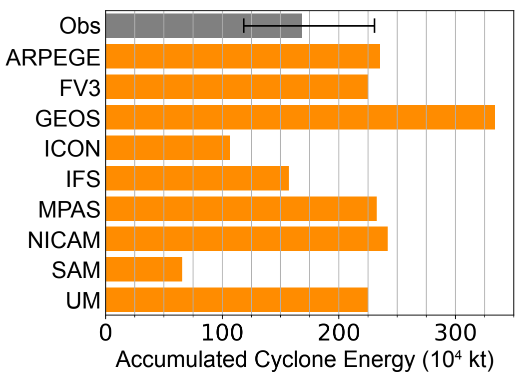

Fig. 6. Accumulated cyclone energy (ACE) from observations (grey) and models (orange). The lower bound of the uncertainty range in observed ACE assumes that all v_{vmax} observations have an error of -5 m s^{-1} or +5 m s^{-1} (upper bound).

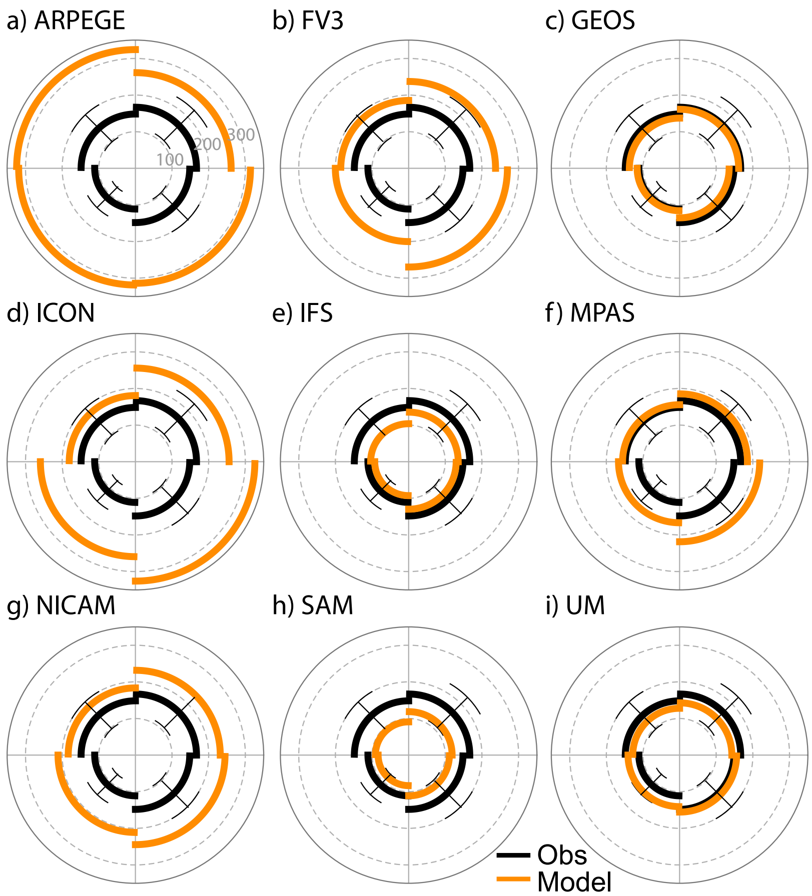

Fig. 7. Average storm size as measured by the median 17 m s^{-1} wind radius for each storm quadrant from observations (black) and models (orange). Dashed grey circles indicate radius intervals of 100 km. The error bars in the observations are based on an error estimate of 50%.

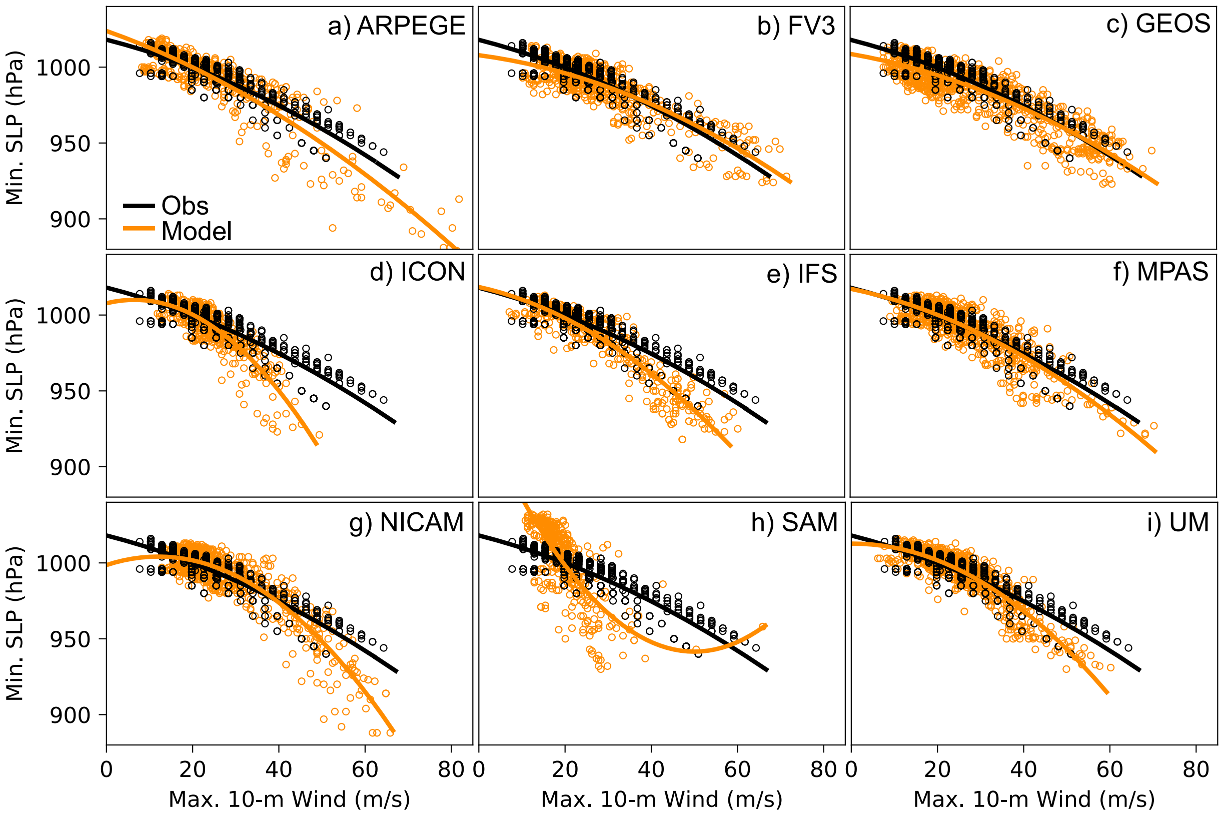

Fig. 8. TC wind-pressure relationships from observations (black) and models (orange). The curves are least-squares tted quadratic functions. Note: the peculiar shape of the fit line in SAM (h) is not caused by the obvious outlier at 65 m s^{-1} and 950 hPa. Excluding this outlier will not change the fit substantially.

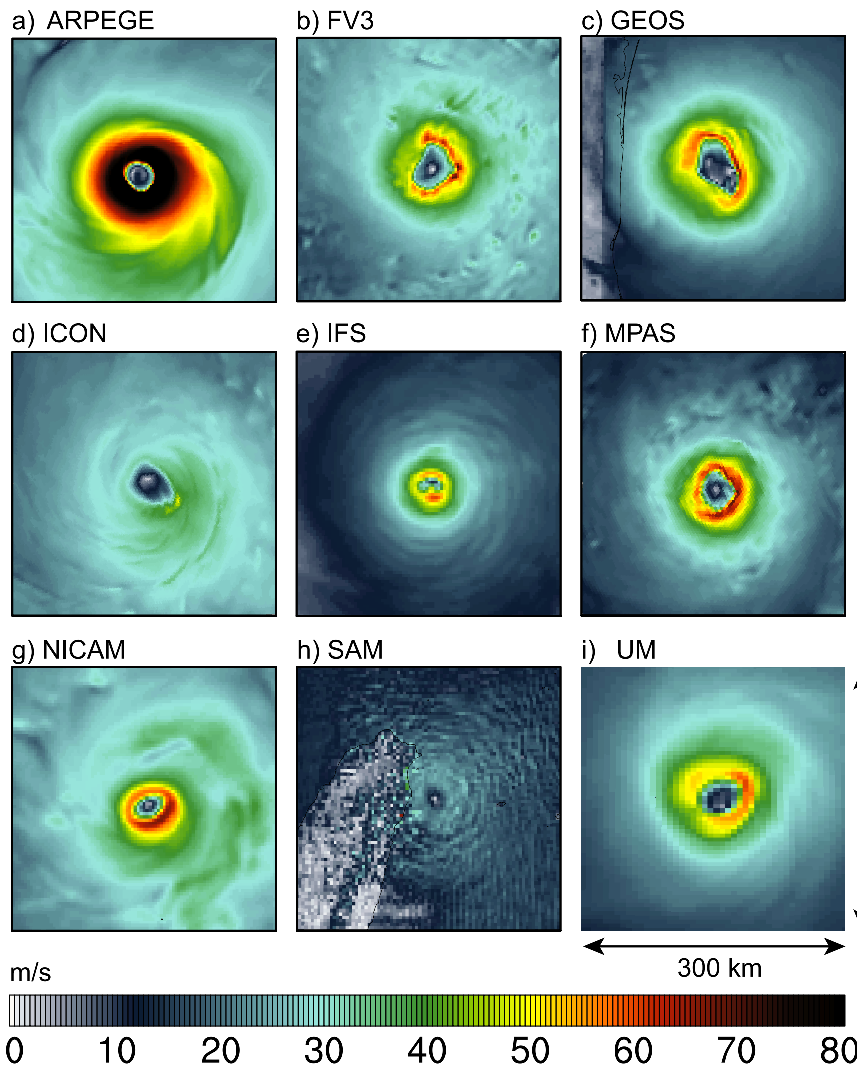
a) ARPEGE
b) FV3
c) GEOS
d) ICON
e) IFS
f) MPAS
g) NICAM
h) SAM
i) UM
300 km
300 km
m/s
0
10
20
30
40
50
60
70
80

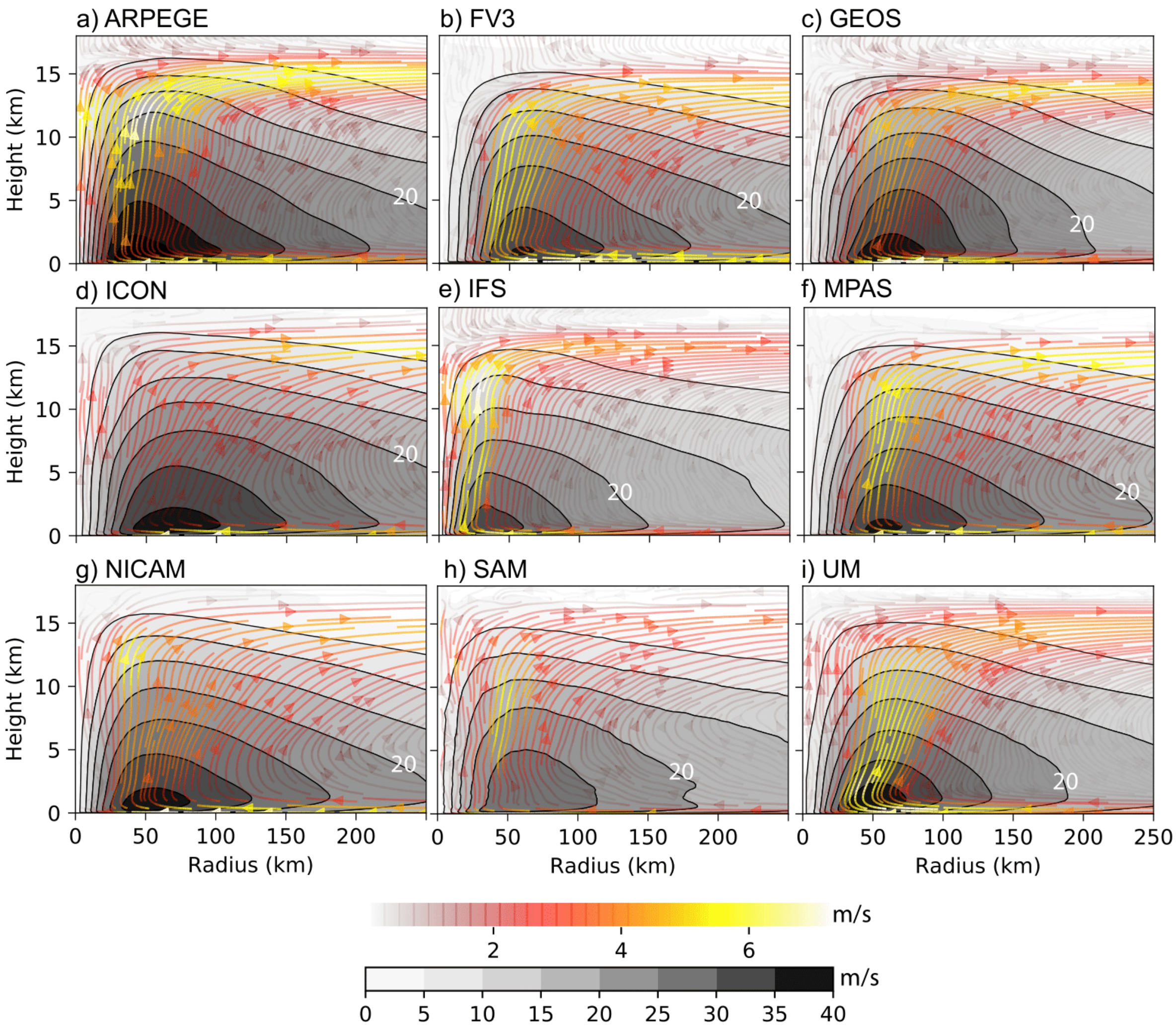

Fig. 10. Radius-height composites of azimuthally-averaged tangential wind speed (grey shading) and radial/vertical flow (colored streamlines) from each model. The 20 m s^{-1}-contour is annotated. The composites include all snapshots where a storm's $v_{max} \geq 33$ m s^{-1}.

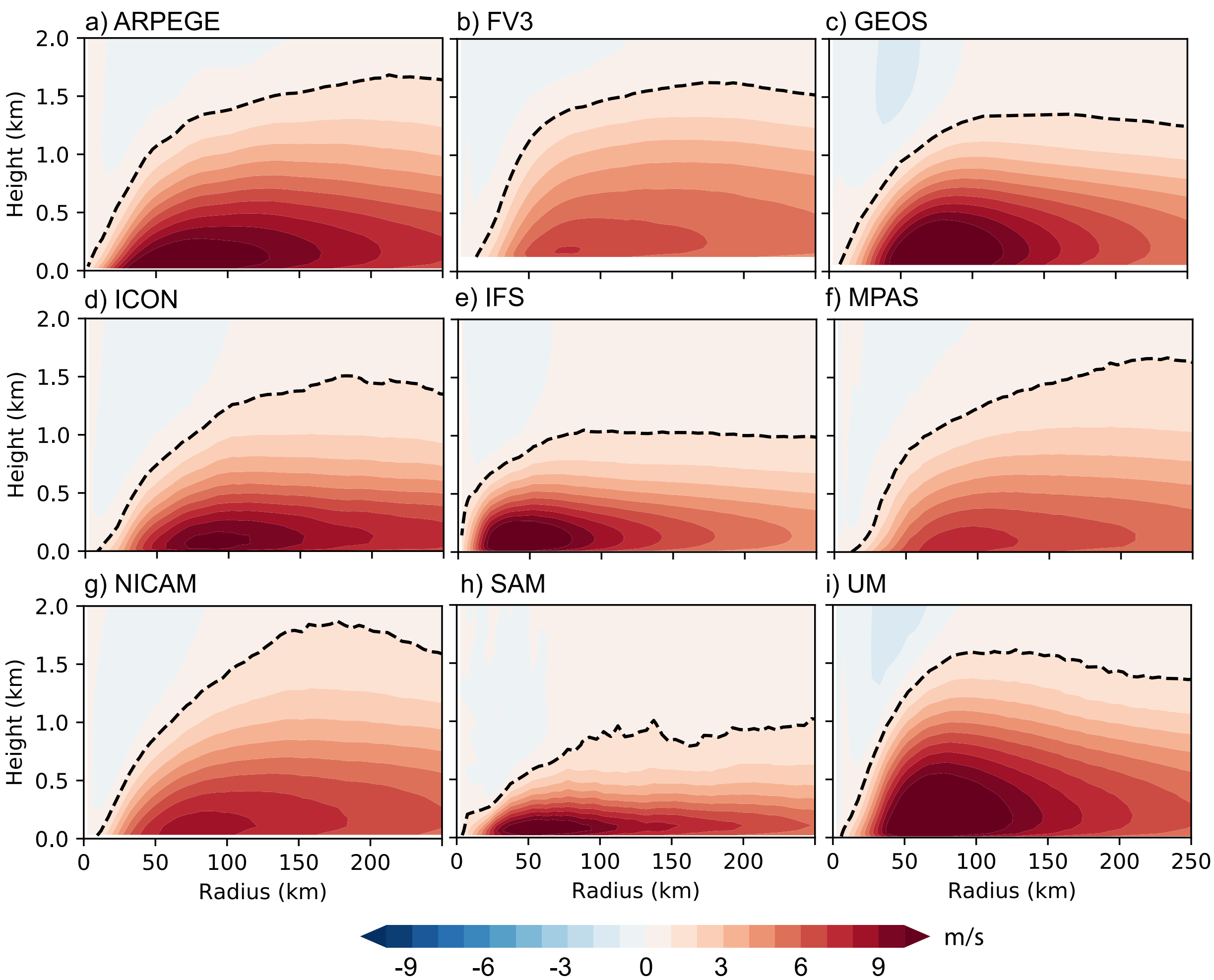

Fig. 11. Radius-height composites of azimuthally-averaged radial wind speed in the lowest 2 km from each model. The dashed black line depicts the inflow layer height, here defined as the layer with radial wind < -1 m s^{-1}. The composites include all snapshots where a storm's $v_{max} \geq 33$ m s^{-1}.

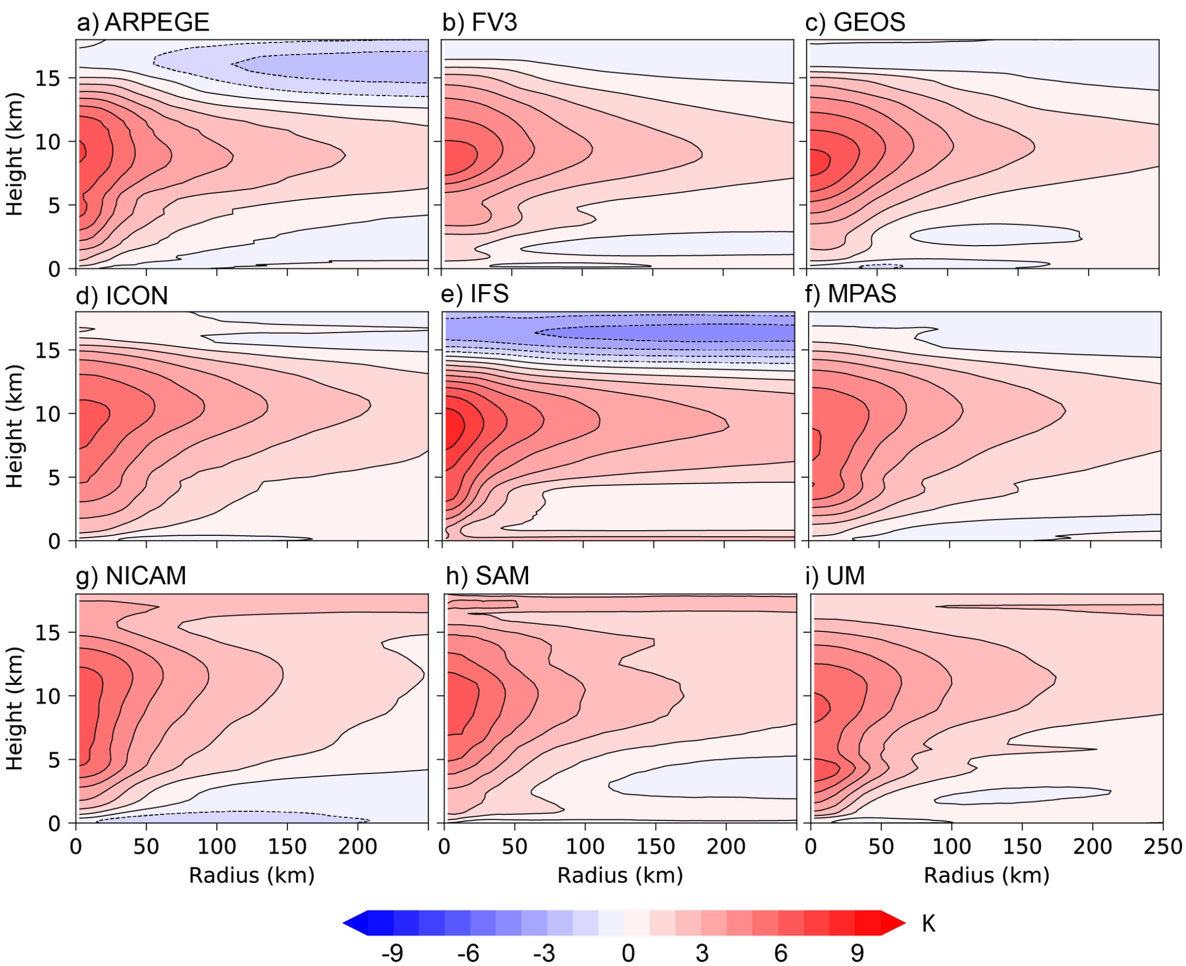

Fig. 12. Radius-height composites of the TC *warm core* from each model, computed as the azimuthally-averaged temperature anomaly with respect to the mean temperature between r = 300–700 km. The composites include all snapshots where a storm's $v_{max} > 32$ m s^{-1}.

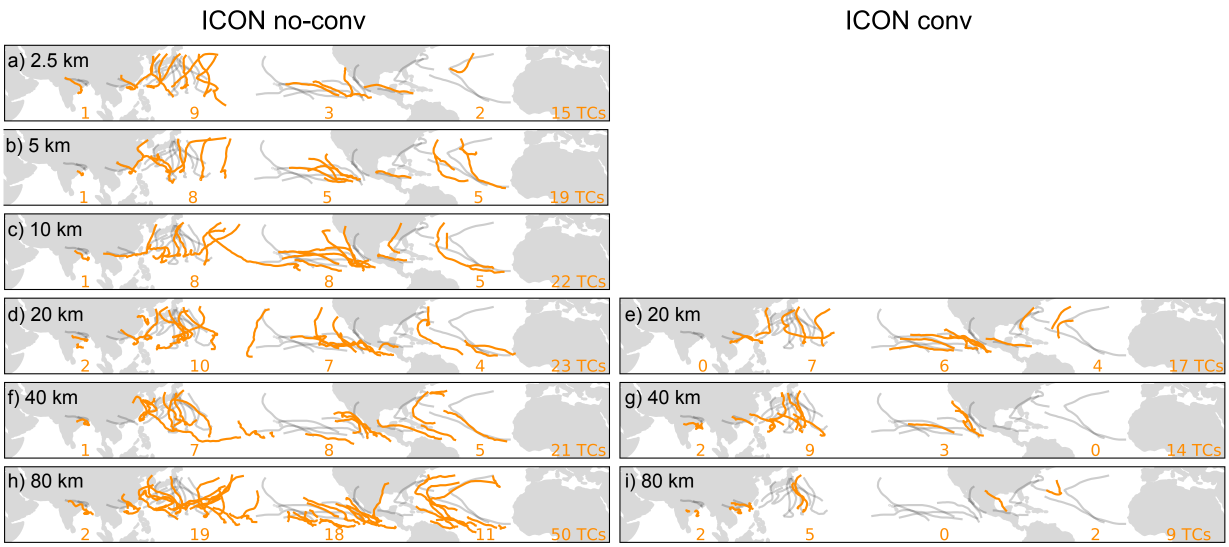

Fig. 13. TC tracks and numbers from various ICON runs (orange) and observations (grey). Left: ICON runs **without** deep convective parameterization, right: ICON runs **with** deep convective parameterization. The model resolution, given in each panel, increases from top to bottom.

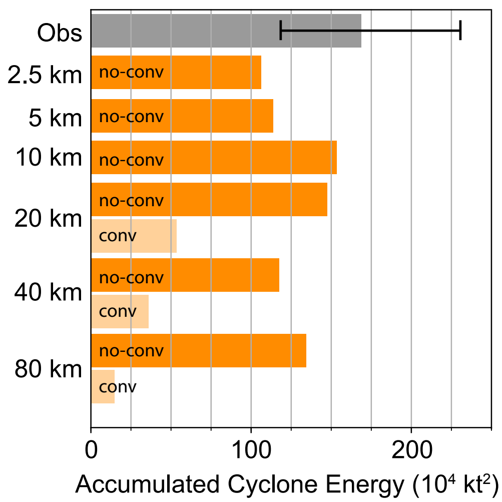

Fig. 14. ACE from observations (grey) and various ICON runs **with** (light orange) or **without** (dark orange) deep convective parameterization. Model resolution increases from top to bottom. The error bars are the lower an upper bounds assuming that all v_{vmax} observations have an error of $\pm$ 5 m s^{-1}.

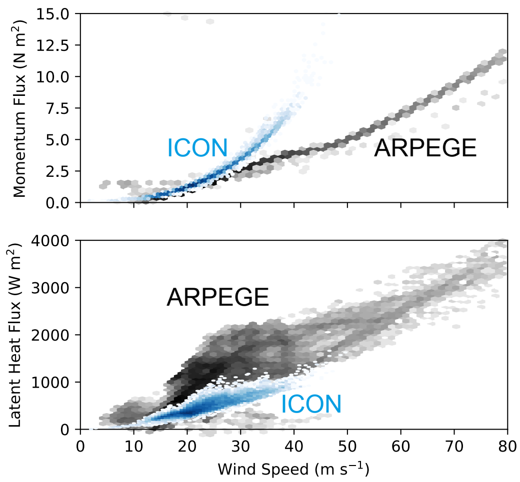

Fig. 15. Momentum flux (top) and latent heat flux (bottom) from ARPEGE and ICON as a function of wind speed. The data are from the same time and domain as the snapshots in Fig. 9. Instead of a raw scatter plot, the data are binned and the color saturation is a measure of points per bin.